AGU PUBLICATIONS

JGR

Journal of Geophysical Research: Space Physics

RESEARCH ARTICLE

10.1002/2016JA022782

Key Points:
- High electron temperatures (e.g., 3000 K) can be obtained in the Martian topside ionosphere without invoking solar wind heating
- The magnetic topology is a key factor in determining electron temperatures and photoelectron fluxes at Mars
- Details of the Martian ionospheric electron temperature are shown to significantly affect electron-ion recombination and hot O production

Correspondence to:
T. E. Cravens,
cravens@ku.edu

Citation:
Sakai, S., et al. (2016), Electron energetics in the Martian dayside ionosphere: Model comparisons with MAVEN data, *J. Geophys. Res. Space Physics*, *121*, 7049–7066, doi:10.1002/2016JA022782.

Received 1 APR 2016
Accepted 25 JUN 2016
Accepted article online 29 JUN 2016
Published online 23 JUL 2016

Electron energetics in the Martian dayside ionosphere: Model comparisons with MAVEN data

Shotaro Sakai[1], Laila Andersson[2], Thomas E. Cravens[1], David L. Mitchell[3], Christian Mazelle[4,5], Ali Rahmati[1,3], Christopher M. Fowler[2], Stephen W. Bougher[6], Edward M. B. Thiemann[2], Francis G. Eparvier[2], Juan M. Fontenla[7], Paul R. Mahaffy[8], John E. P. Connerney[8], and Bruce M. Jakosky[2]

[1]Department of Physics and Astronomy, University of Kansas, Lawrence, Kansas, USA, [2]Laboratory for Atmospheric and Space Physics, University of Colorado Boulder, Boulder, Colorado, USA, [3]Space Science Laboratory, University of California, Berkeley, California, USA, [4]UPS-OMP, IRAP, Université de Toulouse, Toulouse, France, [5]CNRS, IRAP, Toulouse, France, [6]Department of Atmospheric, Oceanic, and Space Sciences, University of Michigan, Ann Arbor, Michigan, USA, [7]NorthWest Research Associates, Boulder, Colorado, USA, [8]NASA Goddard Space Flight Center, Greenbelt, Maryland, USA

Abstract This paper presents a study of the energetics of the dayside ionosphere of Mars using models and data from several instruments on board the Mars Atmosphere and Volatile EvolutioN spacecraft. In particular, calculated photoelectron fluxes are compared with suprathermal electron fluxes measured by the Solar Wind Electron Analyzer, and calculated electron temperatures are compared with temperatures measured by the Langmuir Probe and Waves experiment. The major heat source for the thermal electrons is Coulomb heating from the suprathermal electron population, and cooling due to collisional rotational and vibrational CO_2 dominates the energy loss. The models used in this study were largely able to reproduce the observed high topside ionosphere electron temperatures (e.g., 3000 K at 300 km altitude) without using a topside heat flux when magnetic field topologies consistent with the measured magnetic field were adopted. Magnetic topology affects both suprathermal electron transport and thermal electron heat conduction. The effects of using two different solar irradiance models were also investigated. In particular, photoelectron fluxes and electron temperatures found using the Heliospheric Environment Solar Spectrum Radiation irradiance were higher than those with the Flare Irradiance Spectrum Model-Mars. The electron temperature is shown to affect the O_2^+ dissociative recombination rate coefficient, which in turn affects photochemical escape of oxygen from Mars.

1. Introduction

The goal of the Mars Atmosphere and Volatile EvolutioN (MAVEN) mission is to characterize the loss of atmospheric gas to space and how this has affected the Martian climate through time [*Jakosky et al.*, 2015]. The spacecraft was launched in November 2013 and began orbiting Mars in September 2014.

Atomic oxygen is a key species in atmospheric loss at Mars. The current key path for photochemical loss of neutral oxygen is the dissociative recombination of ionospheric O_2^+, which produces fast oxygen atoms, about half of which have sufficient energy to escape [e.g., *Nagy and Cravens*, 1988; *Fox and Hać*, 2009]. The dissociative recombination coefficient depends on the electron temperature, making the understanding of the electron energetics critical for understanding the loss of oxygen via dissociative recombination at Mars. The electron temperature also plays an important role in the ionospheric dynamics via electron pressure gradients [cf. *Schunk and Nagy*, 2009; *Cravens*, 1997].

Ionospheric plasma is created by photoionization, charge exchange, and electron impact ionization. For example, MAVEN has observed the charge exchange of solar wind protons with the atmosphere, creating fast neutrals in the topside ionosphere which can again charge exchange into protons and deposit heat [*Halekas et al.*, 2015]. Any precipitating neutral or charged particle species (photoelectrons, solar wind particles, or magnetotail electrons) can potentially create secondary ions/electrons. The photoionization is associated with energy deposition in the upper atmosphere by solar extreme ultraviolet (EUV) and soft X-ray photons. The photoelectrons (or suprathermal electrons in general) can heat the plasma as well as produce further ionization or airglow emission [cf. *Fox and Dalgarno*, 1979]. *Sakai et al.* [2015] showed that both external electrons from the magnetosheath and solar soft X-ray irradiance inputs contribute to the high-energy photoelectron flux in the ionosphere and that the photoelectron flux for energies less than 10 eV, related to the ionospheric electron

heating, depends on the ionosphere's electron to neutral density ratio. The electron temperature in the upper atmosphere is controlled by suprathermal/photoelectron heating, by collisional cooling, and by conductive heat transport.

Prior to MAVEN the only in situ measurements of neutral densities or plasma temperatures in the Martian upper atmosphere were provided by the two Viking landers in 1976. The Retarding Potential Analyzer (RPA) on board the Viking 1 (VL1) and the Viking 2 measured plasma densities, velocities, and temperatures in the upper atmosphere [*Hanson et al.*, 1977]. Only the RPA on board the VL1 was successful in measuring the altitudinal profile of electron temperature above 200 km and provided the only in situ measurements of electron temperatures in the Martian ionosphere [*Hanson and Mantas*, 1988]. The RPA electron data were interpreted using three electron populations, i.e., thermal electrons, photoelectrons, and electrons of solar wind origin, with temperatures of about 3000 K, 30,000 K, and 200,000 K above 250 km, respectively [*Hanson and Mantas*, 1988].

Several numerical models of the ion and electron temperatures were able to reproduce the VL1 electron temperatures under certain conditions. Almost all the models suggested that heating by solar radiation was not sufficient and that external heat fluxes at the "top" of the ionosphere are required, just as for the case of the energetics of the Venus ionosphere [*Chen et al.*, 1978; *Johnson*, 1978; *Rohrbaugh et al.*, 1979; *Cravens et al.*, 1980; *Singhal and Whitten*, 1988; *Choi et al.*, 1998; *Matta et al.*, 2014]. For example, one recent temperature model [*Matta et al.*, 2014] required topside heat fluxes of $1.5\times10^{10}\,\mathrm{eV\,cm^{-2}\,s^{-1}}$ for electrons and $2\times10^{7}\,\mathrm{eV\,cm^{-2}\,s^{-1}}$ for ions to match the VL1 data. In the current paper we will compare our model temperatures with temperatures measured by the Langmuir Probe and Waves (LPW) instrument [*Andersson et al.*, 2015] onboard MAVEN and we will show that at least for some conditions, high topside electron temperatures can be obtained without invoking a topside heat flux. Similar analysis has been done at Venus by *Gan et al.* [1990], where they showed that high electron temperatures in agreement with temperatures measured by the Langmuir probe on board the Pioneer Venus Orbiter could be obtained without using topside heat fluxes if a suitable draped magnetic field topology associated with the solar wind interaction is adopted.

In the current paper we compare model electron temperatures with altitude profiles of electron temperatures measured by LPW. The paper also discusses how the photoelectron fluxes measured by the MAVEN Solar Wind Electron Analyzer (SWEA) [*Mitchell et al.*, 2016] and the temperatures measured by LPW are affected by magnetic field topology.

2. MAVEN Measurements

MAVEN data from the dayside portion (inbound legs) of Orbits 819 (3 March 2015) and 873 (13 March 2015) and also outbound Orbit 373 (1 December 2014) are used as our model inputs. Note that we assumed no solar flares of any significance took place during these orbits. These orbits were chosen because they are on the dayside and because the magnetic field exhibits a largely horizontal (i.e., draped) pattern. These data are used for comparisons with data for electron temperature, photoelectron flux, and magnetic field. Figures 1a–1f show the altitude and solar zenith angle (SZA) as a function of time around closest approach for these three orbits. We use data for altitudes between 150 and 500 km and for SZA ranging from 50° to 85° for Orbit 819 (Figure 1d), from 37° to 70° for Orbit 873 (Figure 1e), and from 50° to 100° (Figure 1f) (colored in blue lines of figure) for Orbit 337. Some portion of Orbit 337 is on the nightside, where the SZA is larger than 90°, but our model comparisons will focus on the dayside part of the orbit. The latitude is in ±30° range for Orbit 819 (Figure 1g) and Orbit 873 (Figure 1h) and is in the latitude range of 30° to 70° for Orbit 337 (Figure 1i). The east longitude is between 220° and 290° for all orbits (Figures 1j–1l). The magnetic field measured by the MAVEN magnetometer (MAG) [*Connerney et al.*, 2015] is presented in Figures 1p–1r together with the derived magnetic dip angles (i.e., angle with respect to the horizontal) in Figures 1m–1o. The magnetic dip angle is close to zero, and magnetic fields are also relatively low during these periods.

2.1. Langmuir Probe and Waves (LPW)

The LPW instrument measures the electron density and electron temperature in the Martian ionosphere and can also detect waves that can heat ions, resulting in atmospheric loss [*Andersson et al.*, 2015]. The Langmuir Probe technique (the LP mode of LPW) [*Mott-Smith and Langmuir*, 1926] is used by the LPW instrument to measure both electron densities and temperatures. On the other hand, the wave mode of the LPW instrument can also measure the electron density by observing Langmuir (plasma) waves with frequencies from

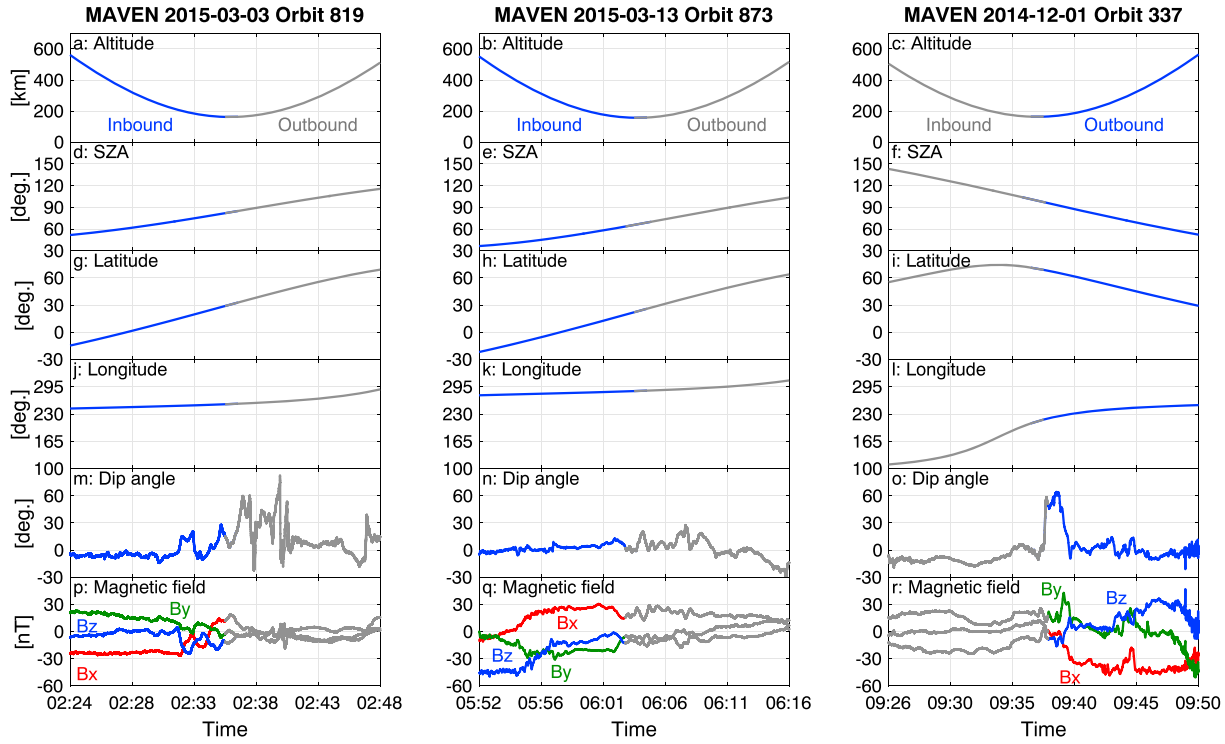

Figure 1. MAVEN orbit information for (left column) Orbit 819, (middle column) Orbit 873, and (right column) Orbit 337. The panels show the (a–c) altitude, (d–f) solar zenith angle, (g–i) latitude, (j–l) east longitude, (m–o) calculated magnetic dip angle, and (p–r) three components of the magnetic field (*x*: red, *y*: green, and *z*: blue) in the MSO (Mars-centered Solar Orbital) coordinate system.

1 Hz to 1 MHz. Finally, the LPW experiment observes low-frequency electrostatic waves that can provide information on where ion heating is taking place. We focus on the Langmuir Probe (LP) technique in the current paper. The LP instrument measures the electrical current generated from the surrounding plasma by sweeping the probe-biased voltages with 128 steps with the maximum sweep range of −50 and 50 V (I–V characteristics), although the details of the sweeps (range and cadence) can vary depending on plasma regime. At periapsis, where the high-resolution measurements are made, the sweep range is ±5 V (cold plasma) with sweep duration of 1 s and a sweep cadence of 1–2 per 4 s [*Andersson et al.*, 2015; *Ergun et al.*, 2015]. The LPW has two independent cylindrical probes with a diameter of 0.0625 cm and with a length of 40 cm long, and the probes have a titanium nitride coating. The probes are situated 7.1 m from the spacecraft main body. The electron density, electron temperature, and spacecraft potential are derived from the I–V curve using an enhanced fitting process [e.g., *Allen*, 1992; *Brace*, 1998]. *Ergun et al.* [2015] describe in detail the LPW fitting process and the treatment of uncertainties in these derived values.

Figure 2 shows electron densities (Figure 2a), temperatures (Figure 2b), and spacecraft (S/C) potential (Figure 2c), which is also measured by I–V characteristics from the LP for Orbits 819, 873, and 337 and including error bars. The electron density is $\approx 6.0 \times 10^4\,\mathrm{cm}^{-3}$ at periapsis, and it decreases with altitude. The measured electron temperature is ≈800 K at periapsis, and it drastically rises to 2000 K for altitudes between 180 km and 300 km. The lowest temperatures a LP can measure are limited by the surface properties of the sensor, and for space measurements it is normally just above 500 K. The two LP sensors have slightly different sensitivities resulting in the lowest temperatures for the respective boom of 600 K and 800 K [*Ergun et al.*, 2015]. Spacecraft charge negatively in ionospheres. For Orbit 819, the LP measured a potential of −1.5 V at 500 km and −0.7 V at lower altitudes (see Figure 2c). On the other hand, the potential for Orbit 873 is lower than that of Orbit 819 (−1.5 V at 350 km and decreasing to −2.5 V near periapsis).

2.2. Solar Wind Electron Analyzer (SWEA)

The SWEA instrument measures electron fluxes for electron energies between 3 eV and 4.6 keV with a time resolution of 2 s [*Mitchell et al.*, 2016]. The instrument is a symmetric, hemispheric electrostatic analyzer

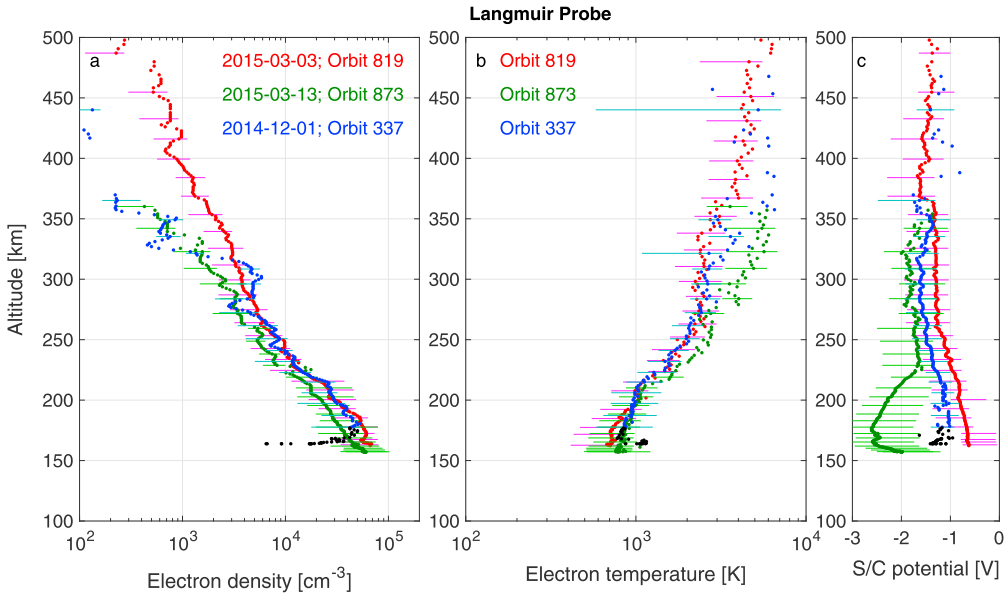

Figure 2. MAVEN/LPW-observed (a) electron densities, (b) electron temperatures, and (c) spacecraft potentials for Orbit 819 (red), Orbit 873 (green), and Orbit 337 (blue). Note that the black dots of Orbit 337 indicate data of the nightside where SZA is larger than 90°.

designed to measure the energy and angular distributions of solar wind electrons and ionospheric photoelectrons in the Martian environment. SWEA selects electrons within a specified energy range by placing a potential difference between two concentric hemispheres [*Mitchell et al.*, 2016, Figure 3]. The center energy of the transmitted electrons is proportional to the potential difference, and the width of the energy response is proportional to energy ($\Delta E/E = 0.17$). The energy resolution is sufficient to resolve the characteristic photoelectron structure near 27 eV [also see *Frahm et al.*, 2006]. More details about the SWEA instrument can be found in *Mitchell et al.* [2016].

3. Model Description

3.1. Photoelectron Production Rates and Solar Irradiance Model

The photoelectron production rate is calculated based on methods described by *Schunk and Nagy* [2009]. Required model inputs include the solar spectrum irradiance, ionospheric neutral and electron densities, and absorption and photoionization cross sections. Background neutral and electron densities are explained in section 3.4.1. Absorption and ionization cross sections for CO_2, CO, N_2, and O are used to determine the production rate of suprathermal electrons and are taken from *Gan et al.* [1990, and references therein] (also see Appendix A and *Sakai et al.* [2015]).

We used the Heliospheric Environment Solar Spectrum Radiation (HESSR) model, which is based on the Solar Irradiance Physical Modeling (SRPM) system [e.g., *Fontenla et al.*, 2011]. We also used the Flare Irradiance Spectral Model (FISM) [*Chamberlin et al.*, 2007], which constructs the solar irradiance spectrum based on the MAVEN EUV Monitor (EUVM) [*Eparvier et al.*, 2015] measurements of the solar irradiance at three wavelength ranges. HESSR solar irradiance is computed from the radiance of a set of features inferred on the solar disk as viewed from Mars. These features are determined from observations made at Earth using daily single snapshot images from the Solar Dynamics Observatory (SDO) near 00:00 UT and are not intended to include flares. We adopted a wavelength (λ) bin size of 0.05 nm for λ less than 6.0 nm and a size of 1.0 nm for λ greater than 6.0 nm. On the other hand, FISM is an empirical model that estimates the solar irradiance at a wavelength from 0.1 to 190 nm at 1 nm resolution. We adopted the FISM-Mars (FISM-M) that estimates irradiances based on the MAVEN EUVM Level 3 data product (Version 04 and Revision 01). Figure 3 shows the solar irradiances from the HESSR and FISM-M for each of the orbits in our current study. The irradiances are almost consistent with each other, but the irradiance for HESSR is higher than for FISM-M between 60 and 100 nm. This affects the production of photoelectrons with energies below ~6 eV (e.g., W. K. Peterson et al., Photoelectrons and

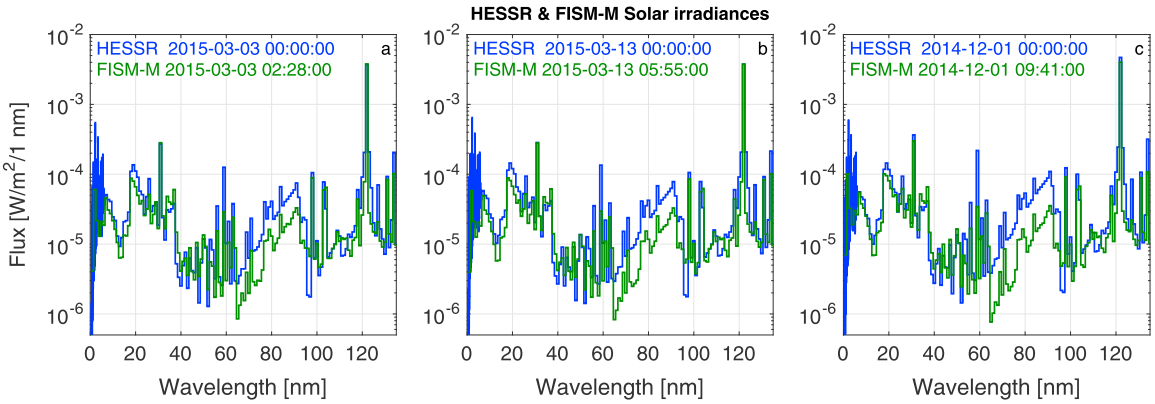

Figure 3. Solar irradiances from HESSR (blue) and FISM-M (green) at Mars are compared for (a) Orbit 819 (3 March 2015), (b) Orbit 873 (13 March 2015), and (c) Orbit 337 (1 December 2014). Note that 1 min cadence data of FISM-M are used for Orbits 819 and 873, and the daily average data are used for Orbit 337. There is no 1 min cadence data for Orbit 337, because MAVEN was not pointed toward the Sun.

solar ionizing radiation at Mars: Predictions vs. MAVEN observations, submitted to *Journal of Geophysical Research*, 2016). The SRPM, which is related to HESSR, has an uncertainty of 20–30% due to the hydrogen continuum. On the other hand, the FISM-M model uncertainty is defined as the model's ability to reproduce SDO/EUV Variability Experiment measurements and is reported to be within 2–11% in this wavelength. Below 6 nm HESSR irradiances are higher than FISM-M irradiances partly because of differences of energy resolution (i.e., $d\lambda = 0.05$ nm for HESSR and $d\lambda = 1$ nm for FISM-M).

3.2. Two-Stream Model and Plasma Heating Rates

The two-stream suprathermal electron transport code (two-stream code) determines electron fluxes, thermal electron heating rates, and electron impact ionization rates. The two-stream code we used to calculate electron fluxes in the Martian ionosphere was originally developed for the Earth by *Nagy and Banks* [1970] and *Banks and Nagy* [1970] and adapted by many researchers for many planets. *Sakai et al.* [2015] used this method to interpret different parts of the electron energy spectrum at Mars. The model determines electron fluxes versus distance s along the field (s is a function of altitude between 100 km and 500 km) and versus energy, ε, between 0.5 eV and 10 keV. Pitch angles in the two-stream model are either up (up flux Φ^+) or down (Φ^-) the magnetic field [e.g., *Richard et al.*, 2011; *Ozak et al.*, 2012; *Sakai et al.*, 2015]. The equations solved are explained in *Sakai et al.* [2015].

Electron impact elastic cross sections are also important for determining the photoelectron energy fluxes at lower energies below 20 eV. We discuss electron impact cross sections for CO_2 and O because CO_2 and O are the dominant species in the Martian thermosphere. The electron impact cross sections for our simulations were adopted from *Gan et al.* [1990, and references therein]. They are compared with other cross sections from *Itikawa* [2002] for CO_2 and *Itikawa and Ichimura* [1990] for O. Our cross sections for CO_2 and O are quite consistent with those of *Itikawa* [2002] and *Itikawa and Ichimura* [1990].

3.3. Energy Equation

The energy equation [*Schunk and Nagy*, 2009; *Richard et al.*, 2011] is as follows:

$$\frac{3}{2}n_s k_B \frac{\partial T_s}{\partial t} + \frac{3}{2}n_s k_B \mathbf{u}_s \cdot \nabla T_s + \frac{3}{2}n_s k_B T_s \nabla \cdot \mathbf{u}_s + \frac{3}{2}k_B (T_s - T_n) S_s + \nabla \cdot (-K_s \nabla T_s) = \sum_j \frac{n_s m_s \nu_{sj}}{m_s + m_j}\left[3k_B (T_j - T_s) + m_j (\mathbf{u}_s - \mathbf{u}_j)^2\right] + Q_s - L_s \quad (1)$$

where a species s denotes thermal electrons $s = e$ or ions (O_2^+) $s = i$, n_s is the number density, k_B is Boltzmann's constant, T_s is the temperature of species s, $\mathbf{u}_s$ is bulk velocity vector of species s, m_s is the mass of species s, t is time, T_n is the neutral temperature, S_s is the mass loading of species s, K_s is the thermal conductivity of species s [*Banks and Kockarts*, 1973], ν_{st} is the momentum transfer collision frequency between species s and j from *Schunk and Nagy* [2009], Q_s is the heating rate, and L_s is the cooling rate. Electrons are heated by Coulomb collisions with suprathermal electrons (calculated by the two-stream photoelectron transport code—see section 3.2), and ions are heated by Coulomb collisions with the thermal electrons and by ion-

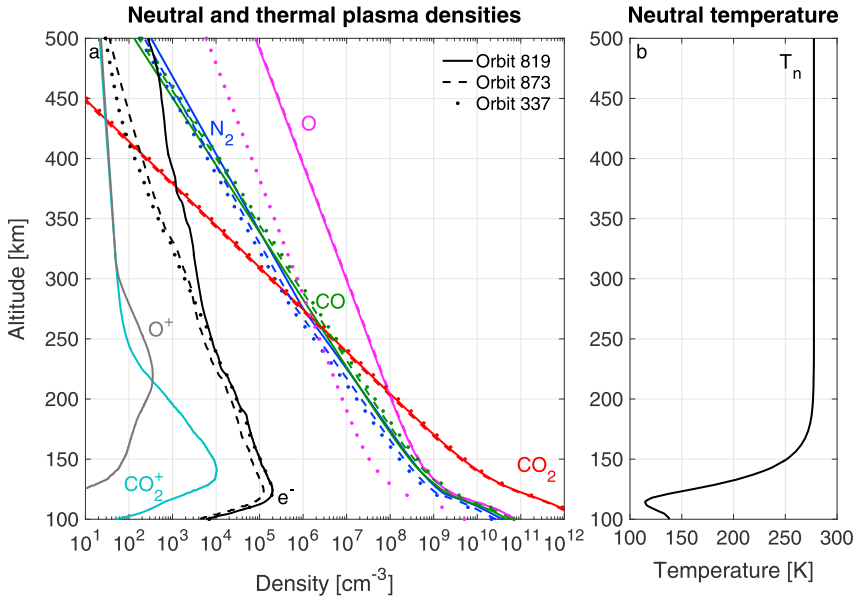

Figure 4. (a) Background neutral, ion, and thermal electron densities for Orbit 819 (solid), Orbit 873 (dashed), and Orbit 337 (dotted) and (b) neutral temperature in the Martian upper atmosphere. The CO_2 (red), CO (green), N_2 (blue), and O (magenta) for neutrals, CO_2^+ (cyan) and O^+ (gray), and thermal electrons (black) are shown.

neutral chemical reactions [e.g., *Cravens et al.*, 1979]. The other ion heat sources are assumed to be the chemical reactions of O^+ and CO_2^+ to O_2^+ based on *Rohrbaugh et al.* [1979]. The electron cooling rates included are vibrational, rotational, and electronic excitational cooling by neutral species, particularly CO_2. Heat is also lost by the thermal electrons via Coulomb collisions with the thermal ion species [*Banks and Kockarts*, 1973; *Gan et al.*, 1990, 1992]. Ions are cooled (or heated if there is drift motion) by elastic collisions with the neutral species. The current paper focuses mainly on the electron energetics, and only preliminary results are shown for the ions.

The plasma temperature distribution could be affected by gyroradius effects if ion and electron gryoradii in the ionosphere are larger than scale height of the ionospheric plasma density distribution. When an electron energy of 10 eV (i.e., photoelectrons) and a magnetic field of 20 nT are assumed, the electron gyroradius is ≈500 m. The plasma scale height in the ionosphere is several kilometers or larger, so we do not need to consider finite gyroradius effects for the electrons. On the other hand, the ions might be affected by gyroradius effects because a typical ion gyroradius is indeed comparable to the plasma scale height. This primarily affects ion heat conduction but ion-ion and ion-neutral collision effects should be dominant in any case in the main ionosphere. Also, the current paper focuses on the electron energetics and temperatures.

3.4. Model Inputs

3.4.1. Background Atmosphere

The neutral (CO_2, CO, N_2, and O) densities are fitted to values measured by the Neutral Gas and Ion Mass Spectrometer (NGIMS) [*Mahaffy et al.*, 2015] for Orbit 819, Orbit 873, and Orbit 373. The density curves are from the University of Michigan's MTGCM (Mars Thermospheric General Circulation Model) for a dayside radial cut at a SZA of 60° and solar cycle maximum [*Bougher*, 2012; *Bougher et al.*, 1988, 1999, 2009], and they were scaled to agree with NGIMS densities (Figure 4a). Our neutral densities agree with the NGIMS densities. The scaling factors are shown in Table 1. Detailed comparisons with NGIMS data are explained in Appendix B, and densities are in good agreement with the NGIMS densities. The MTGCM model is also used for the neutral temperature (Figure 4b). The thermal electron densities used in our model are fits to the LPW data above 170 km for all orbits (colored in black in Figure 4a). For densities below the MAVEN periapsis of about 170 km, MTGCM values were used and matched to MAVEN LPW values at 170 km (see discussion by *Ergun et al.* [2015]). The relative ion densities of CO_2^+ and O^+ (contributing to ion chemical heating) are adopted from the model of *Fox and Haćć* [2009] (cyan for CO_2^+ and gray for O^+ of Figure 4a).

Table 1. The Scaling Factors to Agree With NGIMS Neutral Densities

	CO_2	CO	N_2	O
Orbit 819	2.0	3.0	1.0	4.0
Orbit 873	1.8	3.8	0.7	4.2
Orbit 337	2.3	4.5	0.55	0.3

3.4.2. Magnetic Topology

The magnetic field topology at Mars is complex because solar wind-induced magnetic fields and local crustal magnetic fields are both present [*Acuña et al.*, 1998] although there is no global intrinsic magnetic field. Crustal fields, in particular, are quite complex and linked into the rotation of the planet [e.g., *Brain et al.*, 2003; *Ma et al.*, 2014]. Ionospheric magnetic fields at Mars can be loosely categorized as four general types: (i) draped/induced fields that are open to the solar wind and/or magnetotail at both ends [e.g., *Ma et al.*, 2002, 2004; *Liemohn et al.*, 2006; *Brain et al.*, 2010]; (ii) draped, largely horizontal fields, open at one end to the solar wind and/or magnetotail and attached to Mars at the other end [e.g., *Ma et al.*, 2004; *Liemohn et al.*, 2006]; (iii) crustal fields that are closed at both ends and are attached to the planet [e.g., *Ma et al.*, 2002, 2004, 2014; *Harada et al.*, 2016]; and (iv) crustal fields closed at one end and open to the solar wind or tail at the other end and with significant radial components [e.g., *Ma et al.*, 2002; *Liemohn et al.*, 2006; *Harada et al.*, 2015]. The current paper will consider MAVEN data sets appropriate for topology cases (i) and (ii) on the dayside.

A draped magnetic field line (parabolic) topology is adopted in this model, and the dip angle (i.e., angle with respect to the horizontal) depends on the altitude but is overall less than several degrees for the orbits considered by this paper according to MAG data (Figures 1g–1i). The radius of curvature of field lines at the apex point, where the parabola intersects the line of symmetry and is closest to the center of Mars, is the distance from the apex point to the center of Mars. This parabolic field configuration gives monotonically increasing radial distances with increasing angle from the apex (Figure 5a) [e.g., *Richard et al.*, 2011; *Sakai et al.*, 2015].

Two general cases were considered. (1) The two-stream and energy equations were solved along five different nested field lines whose apex points are the lowest altitudes in separate simulations (Figure 5a). The apex altitudes are at 100, 200, 250, 300, and 350 km, and calculations are performed out to an altitude of 500 km. The SZA for each apex point was made to be consistent with the SZA at the position of MAVEN. (2) A single parabolic field line (Figure 5b) is used, and the two-stream and energy equations are solved for this field line. The apex is placed below the main ionosphere at 100 km. The detailed shape of the field lines is less important than the degree to which the field lines allow electron and/or heat transport between higher altitudes and lower altitudes where the density and collisional losses are larger.

The following model-data comparison cases are considered: (1) insignificant flare conditions, (2) no crustal magnetic fields, and (3) the dayside. The upper boundary condition for the two-stream code is that the down flux is zero (i.e., no solar wind or tail electrons are introduced), and for the plasma temperature code is that temperature gradients are zero (no external heat flow). We assume that the plasma temperatures are equal to the neutral temperature at the lower boundary ($s = 0$) for the single field line, and we assume zero heat flux at $s = 0$ for the nested field lines. The energy equation (equation (1)) is time-dependent, but we obtained

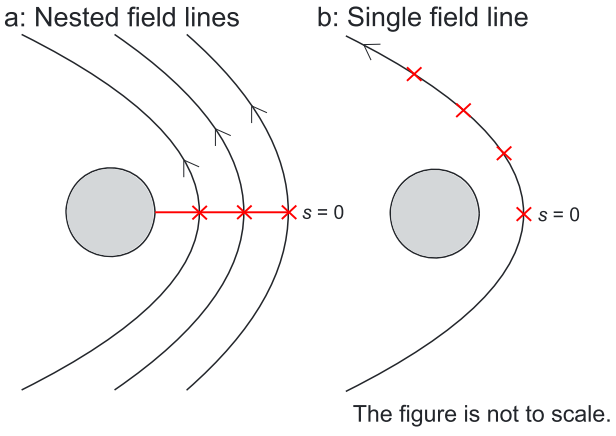

Figure 5. (a) Nested field lines and (b) a single field line are adopted. Simulations are executed along each line, and results at each red cross are discussed in the following sections.

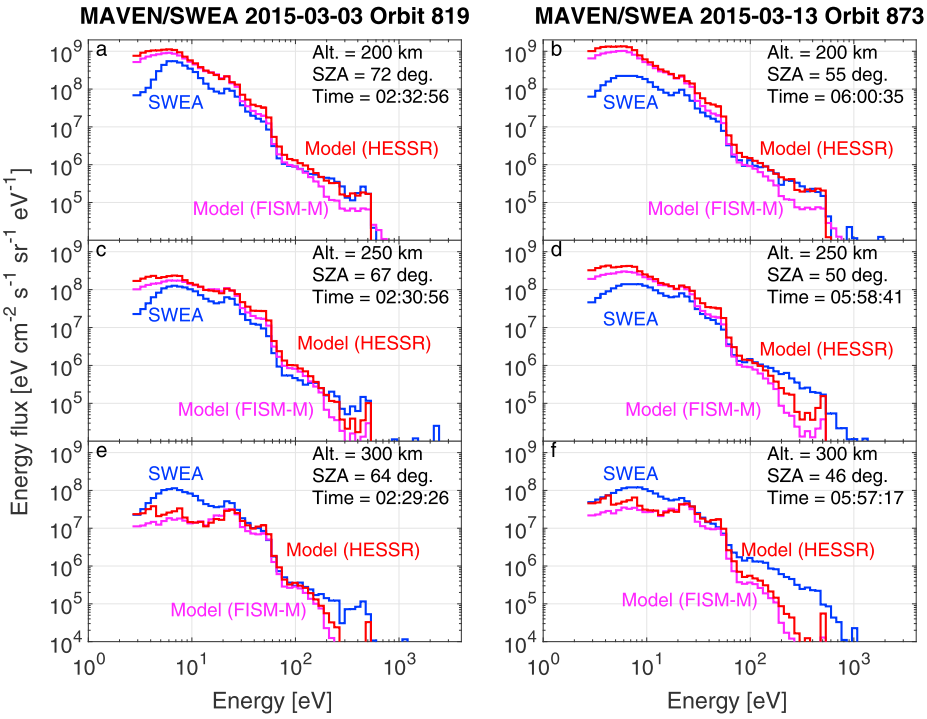

Figure 6. Photoelectron energy fluxes at the altitude of (a and b) 200 km, (c and d) 250 km, and (e and f) 300 km are shown for (left column) Orbit 819 and (right column) Orbit 873. Models using HESSR irradiance (red) and FISM-M irradiance (magenta) are compared with the SWEA measurements (blue).

steady state solutions. The two-stream code [see *Sakai et al.*, 2015] also depends on the thermal electron temperature, so we found the steady state solutions by iterating the two codes.

4. Results

4.1. Photoelectron Energy Fluxes and Electron Heating Rates

Photoelectron energy fluxes averaged over upward and downward directions, with respect to the field line, were computed using two solar irradiances and then compared with SWEA observations for three orbits. The photoelectron energy fluxes are shown as a function of energy at the apex points in Figure 6. Each panel shows the altitude and the solar zenith angle of the apex point, and the time of the observation. For Orbit 819 the model electron fluxes are in agreement with SWEA measurements within a factor of 2 or 3 below 250 km (Figures 6a and 6c). At 300 km the model agrees with SWEA measurements for electron energies between 20 and 100 eV (Figure 6e). Modeled fluxes are lower than SWEA measurements below about 20 eV and above ≈70 eV for an altitude of 300 km (Figure 6e). For energies less than ≈10 eV the photoelectron fluxes also depend on the ionospheric electron to neutral density ratio [*Sakai et al.*, 2015]. The difference between SWEA observations and model results might be due to the input of magnetosheath (tail) electrons at higher energies ($E > 70$ eV) [*Sakai et al.*, 2015].

The thermal electron heating rate due to photoelectrons was obtained from the photoelectron spectra in the two-stream code. Figure 7 shows photoelectron heating rates for each field line (red: apex at 100 km, orange: apex at 200 km, green: apex at 250 km, cyan: apex at 300 km, and purple: apex at 350 km), and the cross symbols indicate apex points for each field line. The heating rate has a peak around the altitude where the ionospheric electron density is at maximum, and it decreases with increasing altitude. Electron heating rates at higher altitudes are lower for the nested field line cases compared to the single field line (red line in Figure 7) connecting to the lower ionosphere case. The reason is that for the latter case photoelectrons produced via photoionization at lower altitudes can stream up to higher altitudes. Electron temperatures are calculated using these heating rates.

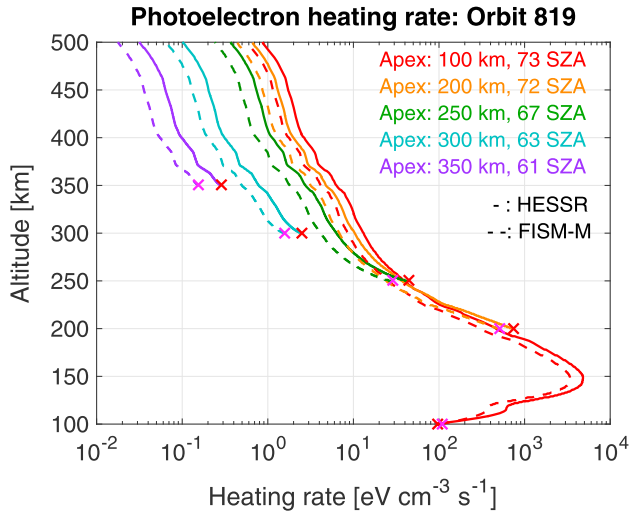

Figure 7. Electron heating rates for apex altitudes of 100 km (red), 200 km (orange), 250 km (green), 300 km (cyan), and 350 km (purple) calculated from photoelectron energy fluxes with HESSR (solid) and FISM-M (dashed) irradiances for Orbit 819.

For Orbit 873 electron fluxes similar to those for Orbit 819 were obtained, although there are some differences. The model fluxes are significantly higher than the SWEA observations at 200 km for lower energies (less than 20 eV) (Figures 6b and 6d) although we used background neutral densities based on NGIMS and electron densities from LPW. The ionospheric electron to neutral density ratio is important for the photoelectron energy fluxes at lower energies, and it is possible that the errors in various inputs accumulated in the simulations. For example, the S/C potential was between −2.5 and −1.7 V in the ionosphere for Orbit 873, which is less than the potential for Orbit 819, so the observed photoelectron fluxes should be slightly less than model values when the S/C potential is negative [*Mitchell et al.*, 2016]. Note that the photoelectron fluxes observed by SWEA were not compensated for the S/C potential in the current paper. Neutral or electron densities also might not be entirely accurate.

Figure 6 shows electron fluxes for cases with different solar irradiances (HESSR and FISM-M), and this provides some measure of the uncertainties associated with the choice of solar flux model. The electron fluxes determined using the HESSR irradiances (red) are higher than those found with the FISM-M irradiances (magenta), in particular above 100 eV. Peterson et al. (submitted manuscript, 2016) showed that the integrated power below 50 nm for HESSR is about 30% higher than that of the FISM-M. The absolute uncertainties of the FISM-M from 6 to 30 nm are better than 10% except for the 28.5 nm bin where it is approximately 15%.

For Orbit 337 the model photoelectron fluxes agree with the SWEA measurements for energies between 20 and 80 eV and for an altitude of 200 km for the nested field lines case (red and magenta of Figure 8a). However, the SWEA fluxes are again somewhat lower than the model fluxes at low energies (below 10 eV in this case) and at higher energies (above 100–200 eV). See the earlier discussion for the other orbits (Orbits 819 and 873). Input of tail electrons might affect the photoelectron distributions for the higher energies and for 200 km and above. The model electron fluxes disagree with observations above 250 km for all energies (red and magenta of Figures 8b and 8c) for the nested field line case. We find that the single field line case does better for Orbit 337 (Figure 5b). The topology is similar to nested field lines, but each parameter is computed along only one field line. The results are shown as the green line in Figures 8a–8c. Below 80 eV the model photoelectron fluxes are now in good agreement with the SWEA measurements. This means that the upward flux must be important for determining the photoelectron fluxes for this orbit. *Sakai et al.* [2015] showed that the photoelectrons created at altitudes below 200 km are transported to high altitudes and significantly affect the flux profiles.

4.2. Calculated Plasma Temperatures and Comparisons With MAVEN Data

LPW measured an electron temperature of about 800 K at the MAVEN periapsis, and the temperature drastically rises to 2000 K between altitudes of 180 km and 300 km and increased further to about 4000 K above 350 km (blue dots in Figure 9). We show the modeled electron temperatures for the nested field line case

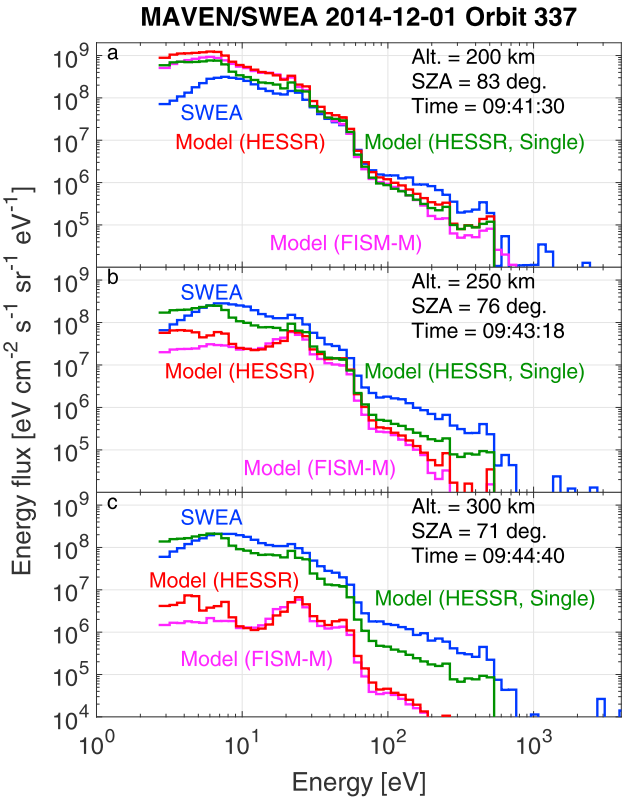

Figure 8. Photoelectron energy fluxes at altitudes of (a) 200 km, (b) 250 km, and (c) 300 km are shown for Orbit 337. Models with HESSR (red) and FISM-M (magenta) irradiances on nested field lines and on a single field line (green) are compared with the SWEA measurements (blue).

obtained by numerically solving equation (1) including the photoelectron heating rate. Figure 9 shows the thermal electron temperature for each nested field line (red: apex of 100 km, orange: apex of 200 km, green: apex of 250 km, cyan: apex of 300 km, and purple: apex of 350 km). The cross symbols show apex points for each field line.

We now discuss the temperatures at the apex points. Model electron temperatures found using the HESSR irradiance (red crosses) are about 50% higher than the temperatures found using the FISM-M irradiance (magenta cross) for Orbit 813 and Orbit 873 (Figures 9a and 9b), which is not surprising given that the HESSR irradiances are overall higher than the FISM-M irradiances, as mentioned in section 4.1. Model temperatures agree reasonably well with the LPW observations above 250 km for Orbit 813 and Orbit 873 (Figures 9a and 9b), although model results with the HESSR irradiance are somewhat higher than the observations at 300 km. Previous models were not able to reproduce temperatures higher than 2000 K without including topside heat fluxes [*Chen et al.*, 1978; *Johnson*, 1978; *Rohrbaugh et al.*, 1979; *Singhal and Whitten*, 1988; *Choi et al.*, 1998; *Matta et al.*, 2014]. For the current paper (and by analogy for *Gan et al.* [1990] for Venus) we succeeded in obtaining high electron temperatures without invoking topside heat fluxes by adopting a suitable magnetic topology. Magnetic topology is clearly an important factor in determining electron temperature and photoelectron distributions in the Martian ionosphere.

For Orbit 873 model electron temperatures agreed with the LPW measurements, although model electron fluxes were higher than SWEA observations below 250 km. A very unrealistic order of magnitude higher electron density was required for the model to agree with the SWEA observations. For this test case photoelectron energy fluxes were in good agreement with SWEA measurements between 200 km and 300 km, and the new electron temperatures were 25–30% lower below 250 km (still within the range of instrumental uncertainty above 300 km). However, the "test" electron density is too high based on the past observations of Viking, MEX, MGS, and also MAVEN even if model results did agree with the SWEA measurements. As another sensitivity test for 10 eV or so suprathermal fluxes we varied the CO_2 vibrational cross sections in the code. There were

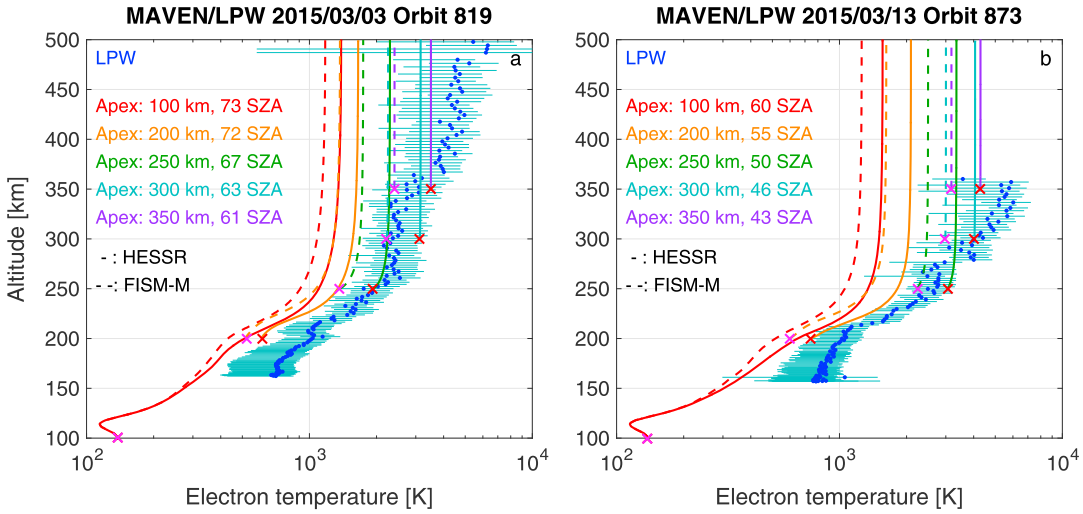

Figure 9. Model electron temperatures at 100 km (red), 200 km (orange), 250 km (green), 300 km (cyan), and 350 km (purple) are compared with the LPW observations (blue) with error bars (cyan). The variation of temperature with different solar irradiances (HESSR: solid, FISM-M: dashed) is also shown for each orbit: (a) Orbit 819 and (b) Orbit 873. The crosses denote the apex points for each field line.

some differences between our cross sections and recent ones of *Itikawa* [2002], but model results did not change much. We cannot resolve the issue of model-SWEA low-energy comparisons in the current paper.

Below 200 km our model electron temperatures are noticeably lower than the LPW measurements. Theoretically, one expects the electron and ion temperatures to both equal the neutral temperature in the lower ionosphere where the neutral densities (and cooling rates) are large [cf. *Schunk and Nagy*, 2009]. However, Langmuir probes are known to have difficulties measuring temperatures below about 500 K and surface contamination might make the performance worse than this [cf. *Ergun et al.*, 2015].

For Orbit 337 we showed the photoelectron fluxes for nested field lines as well as for a single field line (Figure 8). Electron temperatures were also obtained in these two cases for the HESSR irradiances. Figure 10 shows the electron temperature on each nested field line (red: apex of 100 km, orange: apex of 200 km, green: apex of 250 km, cyan: apex of 300 km, and purple: apex of 350 km) and for a single line (black). The red cross symbols show apex points on each field line, and the brown cross symbols show each altitude

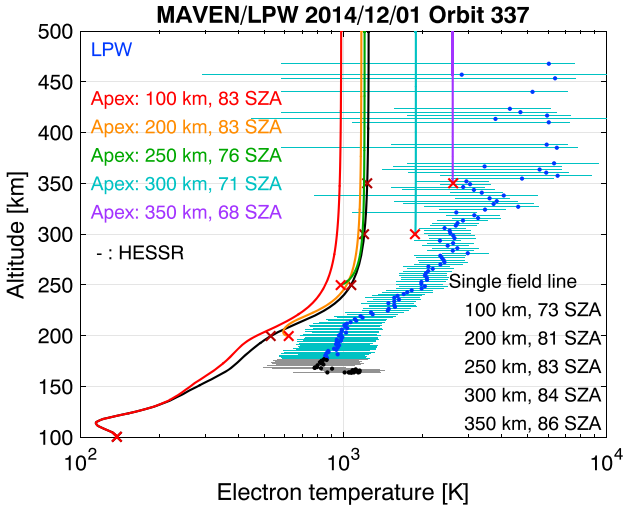

Figure 10. The comparison of model electron temperatures with the LPW measurements for Orbit 337. Same colors and lines as Figure 9. The black line denotes the electron temperatures in the case of a single field line, and the black dots indicate data from the nightside.

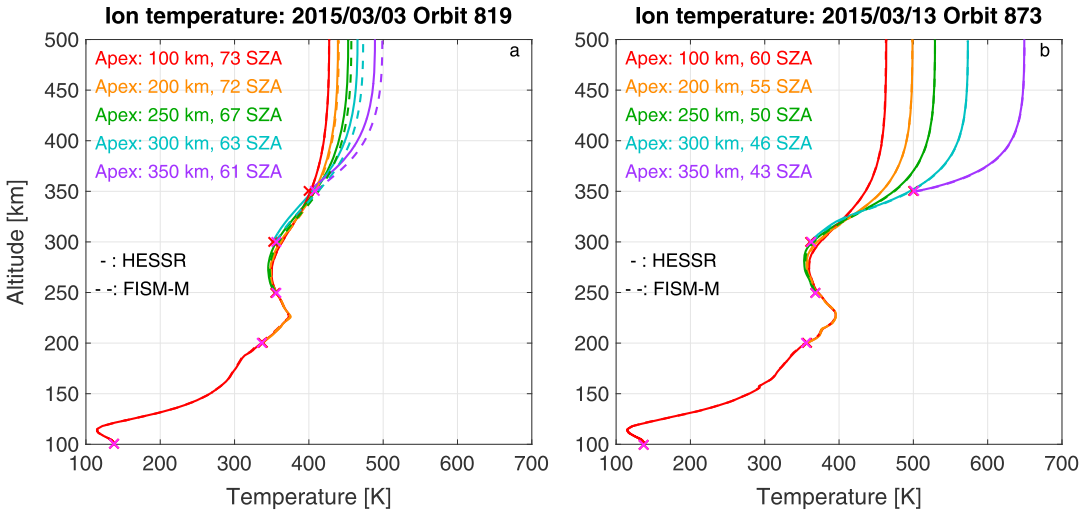

Figure 11. Model ion temperatures in the ionosphere. Same colors and lines as Figure 9. These are preliminary results.

on a single field line. Model electron temperatures are lower than the LPW observations in both cases and, in particular, much lower for a single field line although the photoelectron fluxes agree with the SWEA measurement at low energies. The reason might be the influence of tail electrons. Enhanced magnetosheath electrons could be a heat source for thermal electrons because they increase the photoelectron fluxes at high energies. Or perhaps, a single draped line topology might not be applicable, and instead, nested field lines might be better.

4.3. Modeled Ion Temperatures

Our ion temperature results are preliminary in that the ion energetics depend, particularly at higher altitudes, on the overall dynamics, which we neglect here and which generally require global models to properly characterize [e.g., *Ma et al.*, 2004]. Ion temperatures were found by solving the coupled electron and ion energy equations (equation (1) shown earlier). In particular, this was done for the nested field lines case under the assumption that O_2^+ is the dominant ion species at all altitudes. Figure 11 shows the calculated ion temperatures for Orbit 819 (Figure 11a) and Orbit 873 (Figure 11b). The temperature is about 350 K for both cases, and it increased to 400 K for Orbit 819 and to 500 K for Orbit 873 at 350 km. The ion temperature strongly depends on the electron temperature, so the ion temperatures for Orbit 873 are higher than for Orbit 819 because the Orbit 873 electron temperatures are higher (Figure 9). The ion temperatures are also enhanced at ≈220 km altitude because of the heating by the chemical reactions of O^+ and CO_2^+ to O_2^+ (as originally suggested by *Rohrbaugh et al.* [1979]). The ion temperatures were not affected by the HESSR-FISM differences of solar irradiances. Our modeled temperatures are somewhat lower than the Viking RPA observations [*Hanson et al.*, 1977]—the Viking ion temperatures were 1000 K at 250 km and 3000 K at 350 km. Past models reproduced such high temperatures by including ion heat fluxes at the top [e.g., *Matta et al.*, 2014]. Note that we succeeded in reproducing the electron temperature without topside heat fluxes, but evidently, this does not work for the ions. More work is clearly needed for the ion energetics.

Our electron temperature results are not sensitive to some increases of ion temperature because the main electron heating is due to photoelectrons and the main cooling is due to collisions with neutrals. Relative ion densities from *Fox and Hać* [2009] were used for the ion chemical heating in the model. It is expected that the ion densities based on MAVEN observations such as the NGIMS or SupraThermal and Thermal Ion Composition [*McFadden et al.*, 2015] instruments should be adopted for simulations, but in this work we mainly focus on the electron energetics in the Martian ionosphere.

5. Discussion

5.1. Relationship Between Photoelectrons and Magnetic Topology

We obtained photoelectron distributions for two cases: (1) photoelectrons dominated by a magnetic topology associated with nested field lines (Orbit 819 and Orbit 873; Figure 6) and (2) photoelectrons dominated by

transport from low altitudes on a single field line (Orbit 337; Figure 8). We showed the modeled electron temperatures agreed with the LPW measurements when nested field lines are considered because MAVEN (and the LPW) could be encountering different field lines. Photoelectron fluxes strongly depend on the position and topology of magnetic field lines. On the other hand, for Orbit 337 model-data comparisons were better for a single field line topology than for nested field lines. The single field line case facilitates electron transport between low and high altitudes. The geographic position (i.e., day or night, region of crustal magnetic field) as well as solar wind conditions should be relevant to the magnetic topology. MAVEN passed through the longitude range of 220° to 290° for both field line cases, while it moved from −20° to 30° latitude for the orbits where the nested field lines work best and from 70° to 30° for the case for which the single field line worked best (Orbit 337).

The magnetic topology is different for a draped-induced field line open at both ends and a draped horizontal field open at one end to the solar wind and/or magnetotail and attached to Mars at the other end. Low to high altitude connectivity is different for field lines open at both ends and field lines open at one end and connected to Mars (i.e., crustal fields) at the other end [*Krymskii et al.*, 2002; *Brain et al.*, 2003]. Photoelectrons generated near the ionospheric peak (≈150 km altitude) are easily transported to high altitudes along a field line [*Liemohn et al.*, 2006; *Sakai et al.*, 2015], and they should be important for the magnetically connected case. The magnetotail (or magnetosheath) can also act as a source of suprathermal electrons for the ionosphere [*Liemohn et al.*, 2006], so it is possible that the enhancement of energy fluxes above 70 eV is due to tail electrons for Orbit 337 [*Sakai et al.*, 2015].

5.2. The Effect of the Solar Wind on the Energetics

Solar wind or magenetosheath electrons can potentially penetrate into the Martian ionosphere along open magnetic field lines. We now discuss the possible effects of the solar wind on suprathermal electron fluxes and electron temperatures in the ionosphere.

External suprathermal electrons (i.e., nonphotoelectrons such as solar wind electrons) do not appear to be present in the SWEA measurements below 250 km, and our model photoelectron fluxes (without solar wind inputs) agree well with (or were a little higher than) SWEA measurements below ≈15 eV. The agreement below 250 km seems to indicate that the electron distributions are not affected by the solar wind below 250 km. However, our model fluxes were lower than SWEA measurements at an altitude of 300 km, and perhaps, the reason for lower model suprathermal electron fluxes above 70 eV could be due to magnetosheath electrons.

Any penetration of the solar wind motional electric field into the ionosphere should not affect the electron energetics because electron velocities are much higher than the convection (or $E \times B$) drift velocity, but this type of effect might indeed affect the ion energetics. However, the current paper does not focus on ion dynamics as mentioned in section 4.3.

5.3. O_2^+ Dissociative Recombination: Implication for Photochemical Escape

The dissociative recombination of ionospheric O_2^+ ions with electrons is one of the key processes for atmospheric loss at Mars [e.g., *Nagy and Cravens*, 1988]. *Rahmati et al.* [2015] suggested that comparisons made between modeled energetic oxygen pickup ion fluxes and those measured by the Solar Energetic Particle instrument onboard MAVEN can provide constraints on exospheric models and their associated neutral oxygen (or photochemical) escape rates. The dissociative recombination rate coefficient for O_2^+ is given by $\alpha = 2.4 \times 10^{-7}\ (300/T_e)^{0.70}$ [*Peverall et al.*, 2001], where T_e denotes the electron temperature. We compare the dissociative recombination rate coefficients for different electron temperatures discussed in this paper. Figure 12 shows the O_2^+ dissociative recombination rate coefficient as a function of altitude for two model cases, which directly use LPW data (Orbits 819 and 873). Values of α calculated using model electron temperature are higher than α values found using the LPW temperatures by a factor of 2 at 150 km near the ionospheric peak and are 30–40% higher near the exobase (200 km). In particular, the model gives $\alpha = 2 \times 10^{-7}\ \mathrm{cm^3\ s^{-1}}$ at 150 km and $\alpha = 1.3 \times 10^{-7}\ \mathrm{cm^3\ s^{-1}}$ near the exobase. Model ionospheres and photochemical loss rates depend on these values, and loss models should recognize the differences [*Fox and Hać*, 2009; *Lillis et al.*, 2015].

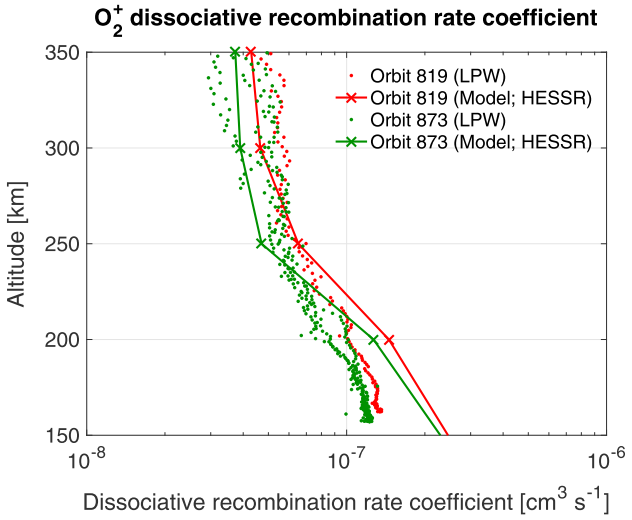

Figure 12. Comparisons of O_2^+ dissociative recombination coefficients calculated from electron temperature between model (solid) and LPW (dots) for Orbits 819 (red) and 873 (green).

6. Summary

Photoelectron fluxes and thermal electron temperatures in the Martian ionosphere were studied using model comparisons with MAVEN SWEA and LPW data for conditions with insignificant solar flare, no crustal magnetic field, and for the dayside. We succeeded in producing high electron temperatures (e.g., 3000 K) at high altitudes without requiring heat fluxes from the top. The topology and position of magnetic field lines were shown to be important factors in determining the profile of electron temperature and also photoelectron distributions. Model electron temperatures associated with photoelectron fluxes agreed with the LPW measurements when nested field lines were considered for Orbit 819 and Orbit 873. On the other hand, the photoelectron fluxes are in good agreement with the SWEA measurements (although thermal electron temperatures were somewhat lower than the LPW observations), when a single field line was used for Orbit 337, and that allowed vertical transport of photoelectrons.

The difference between using HESSR and FISM-M solar irradiances was also investigated. The photoelectron fluxes with the HESSR irradiance were higher than those found using the FISM-M irradiances (in particular for energies above 100 eV) because the HESSR irradiances are higher for the 65–90 nm range. The electron temperatures found using HESSR were also higher than for FISM-M for the same reason.

The O_2^+ dissociative recombination rate coefficients were found for both model temperatures and for temperatures measured by LPW, and differences of about 30–100% were found. These differences will affect ionospheric density calculations and hot oxygen atom production rates.

In the future more model-SWEA and -LPW comparisons including the crustal magnetic fields would provide constraints on ionospheric heat processes for complex magnetic fields such as a combination of solar wind and crustal fields. Electron distributions are dependent on the magnetic topology in the Martian ionosphere. For example, electron densities and low-energy photoelectron fluxes should increase on dayside closed crustal fields, whereas for field lines closed at one end on the dayside and open at the other, photoelectrons can escape, leading to a lowering of the overall fluxes and thus decreasing the heating rate of thermal electrons. Perhaps these effects can be analyzed in the future using SWEA, LPW, and model-data comparisons. We restricted ourselves to the easier draped field line case in the current paper.

Appendix A: Absorption and Photoionization Cross Sections

We consider four photoionization reactions for photoelectron productions:

$$N_2 + h\nu \rightarrow N_2^+ + e^- \quad \text{(A1)}$$

$$CO_2 + h\nu \rightarrow CO_2^+ + e^- \quad \text{(A2)}$$

$$CO + h\nu \rightarrow CO^+ + e^- \quad \text{(A3)}$$

$$O + h\nu \rightarrow O^+ + e^- \quad \text{(A4)}$$

Photoelectron production rates are given by [*Schunk and Nagy*, 2009]

$$P_e(E,\chi,z) = \sum_i \sum_s n_s(z) \int_0^{\lambda_{si}} I_\infty(\lambda) \exp[-\tau(\lambda,\chi,z)] \sigma_s^i(\lambda) p_s(\lambda, E_i) d\lambda \quad \text{(A5)}$$

where P_e is the photoelectron production rate, I_∞ is the solar flux, $\sigma_s{}^i$ is the photoionization cross section, p_s is the branching ratio for a given final ion state with ionization level E_i, $E = E_\lambda - E_i$, E_λ is the energy corresponding to

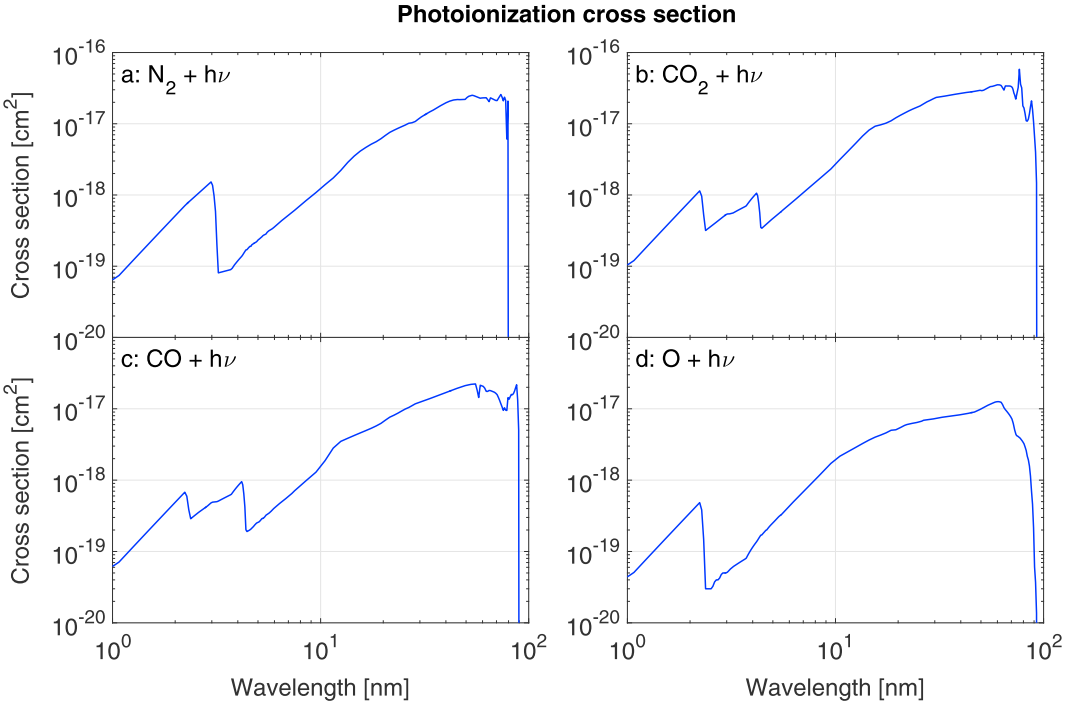

Figure A1. Photoionization cross sections for (a) N_2^+, (b) CO_2^+, (c) CO^+, and (d) O^+.

wavelength λ, λ_{si} is the ionization threshold wavelength for neutral species s, τ is the optical depth, z is the altitude, χ is the solar zenith angle, and subscript $\imath$ indicates the ion component. Figure A1 shows the photoionization cross sections obtained using the photoionization rates from *Gan et al.* [1990]. We used the solar irradiances of HESSR and FISM-M. The optical depth depends on photoabsorption cross sections and column densities. Figure A2 shows the photoabsorption cross sections from *Gan et al.* [1990].

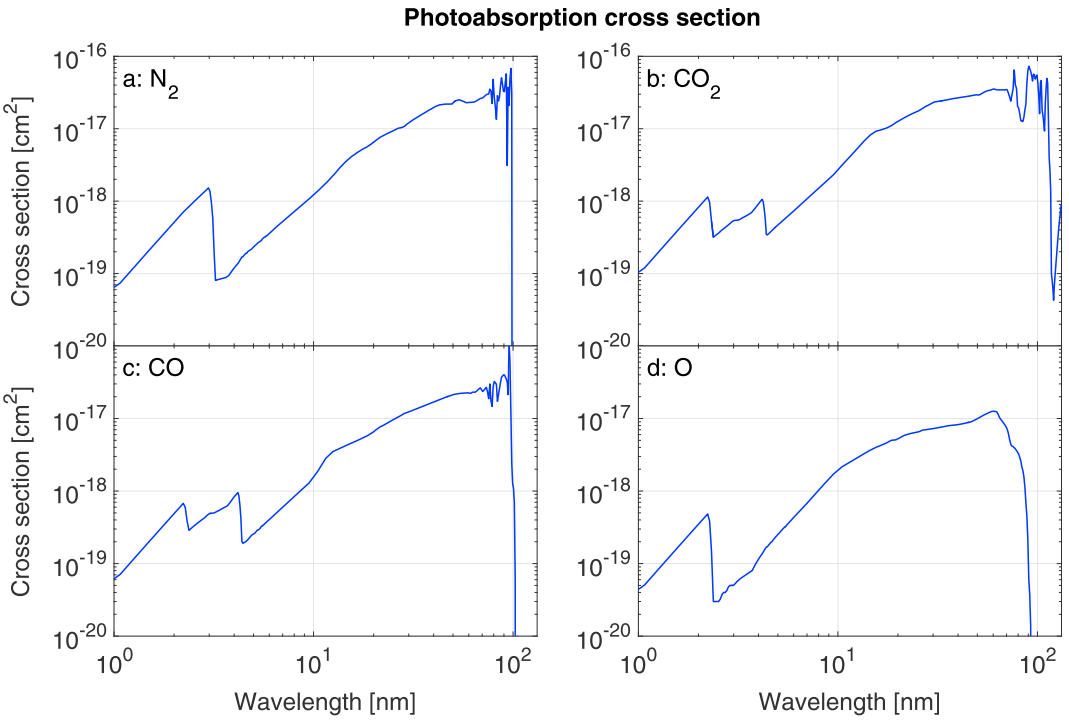

Figure A2. Photoabsorption cross sections for (a) N_2, (b) CO_2, (c) CO, and (d) O.

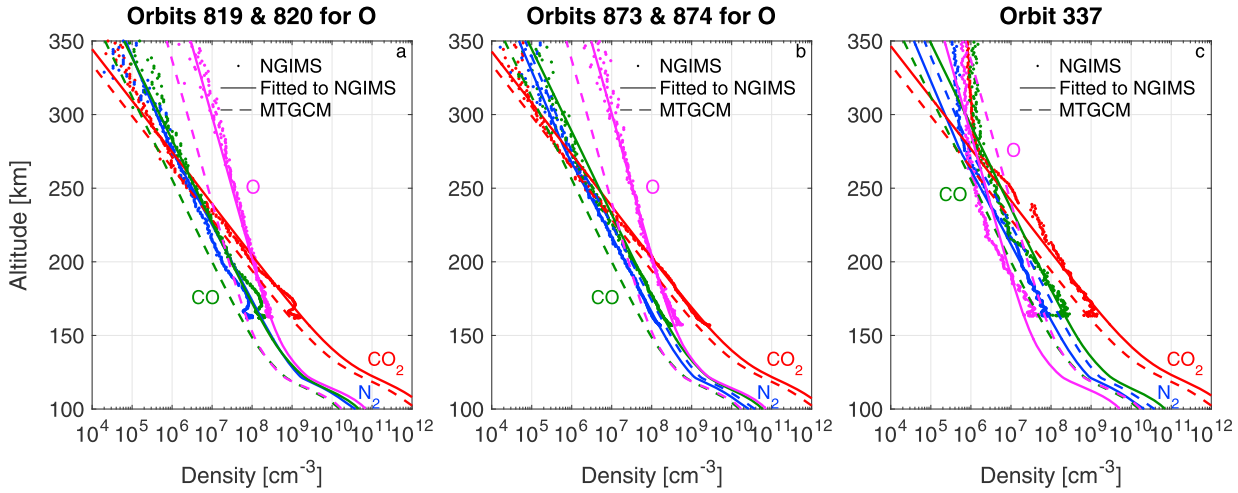

Figure B1. Neutral densities fitted to NGIMS (solid), NGIMS (dots), and MTGCM (dashed) are compared for (a) Orbit 819, (b) Orbit 873, and (c) Orbit 337. The CO_2 (red), CO (green), N_2 (blue), and O (magenta) are included in this model.

Appendix B: Background Neutral Atmosphere Fitted to NGIMS

Neutral densities fitted to NGIMS are used for our simulations. Figure B1 shows the NGIMS-observed neutral densities (dots), neutral densities fitted to NGIMS by multiplying appropriate factors by MTGCM (solid), and original neutral densities of MTGCM (dashed) for Orbit 819 and Orbit 820 for oxygen (Figure B1a), Orbit 873 and Orbit 874 for oxygen (Figure B1b), and for Orbit 337 (Figure B1c). Atomic oxygen was not measured for Orbit 819 and Orbit 873 because NGIMS measured species using only the closed source. Atomic oxygen is only detectable in the open source mode. We used the oxygen densities measured on Orbit 820 and Orbit 874 in our simulations.

Acknowledgments
All data shown in the figures can be obtained from the corresponding author. MAVEN data are in the Planetary Data System. This work was supported by NASA grant NNH10CC04C to the University of Colorado and by subcontract to the University of Kansas. The MAVEN project is supported by NASA through the Mars Exploration Program. This work was also partially supported by CNES for the part based on observations with the SWEA instrument onboard MAVEN.

References

Acuña, M. H., et al. (1998), Magnetic field and plasma observations at Mars: Initial results of the Mars Global Surveyor mission, *Science*, *279*, 1676–1680, doi:10.1126/science.279.5357.1676.

Allen, J. E. (1992), Probe theory – The orbital motion approach, *Phys. Scr.*, *45*, 497, doi:10.1088/0031-8949/45/5/013.

Andersson, L., R. E. Ergun, G. T. Delory, A. Eriksson, J. Westfall, H. Reed, J. McCauly, D. Summers, and D. Meyers (2015), The Langmuir Probe and Waves (LPW) Instrument for MAVEN, *Space Sci. Rev.*, *195*, 173–198, doi:10.1007/s11214-015-0194-3.

Banks, P. M., and A. F. Nagy (1970), Concerning the influence of elastic scattering upon photoelectron transport and escape, *J. Geophys. Res.*, *75*, 1902–1910, doi:10.1029/JA075i010p01902.

Banks, P. M., and G. Kockarts (1973), *Aeronomy*, Academic Press, New York.

Bougher, S. W. (2012), Coupled MGCM-MTGCM Mars thermosphere simulations and resulting data products in support of the MAVEN mission, *JPL/CDP Rep.*, pp. 1–9, 6 Aug.

Bougher, S. W., R. E. Dickinson, R. G. Robie, and E. C. Ridley (1988), Mars Thermospheric General Circulation Model: Calculations for the arrival of Phobos at Mars, *Geophys. Res. Lett.*, *15*, 1511–1514, doi:10.1029/GL015i013p01511.

Bougher, S. W., S. Engel, R. G. Robie, and B. Foster (1999), Comparative terrestrial planet theremosphere 2. Solar cycle variation of global structure and winds at equinox, *J. Geophys. Res.*, *104*, 16,591–16,611, doi:10.1029/1998JE001019.

Bougher, S. W., A. Valeille, M. R. Combi, and V. Tenishev (2009), Solar cycle and seasonal variability of the Martian thermosphere-ionosphere and associated impacts upon atmospheric escape, *SAE Int. J. Aerosp.*, *4*(1), 227–237, doi:10.4271/2009-01-2396.

Brace, L. H. (1998), Langmuir probe measurements in the ionosphere, in *Measurement Techniques in Space Plasmas: Particles*, *Geophys. Monogr. Ser.*, vol. 102, edited by R. F. Pfaff, J. E. Borovsky, and D. T. Young, pp. 23–36, AGU, Washington, D. C.

Brain, D. A., F. Bagenal, M. H. Acuña, and J. E. P. Connerney (2003), Martian magnetic morphology: Contributions from the solar wind and crust, *J. Geophys. Res.*, *108*(A12), 1424, doi:10.1029/2002JA009482.

Brain, D. A., et al. (2010), A comparison of global models for the solar wind interaction with Mars, *Icarus*, *206*, 139–151, doi:10.1016/j.icarus.2009.06.030.

Chamberlin, P. C., T. N. Woods, and F. G. Eparvier (2007), Flare Irradiance Spectral Model (FISM): Daily component algorithms and results, *Space Weather*, *5*, S07005, doi:10.1029/2007SW000316.

Chen, R. H., T. E. Cravens, and A. F. Nagy (1978), The Martian ionosphere in light of the Viking observations, *J. Geophys. Res.*, *83*, 3871–3876, doi:10.1029/JA083iA08p03871.

Choi, Y. W., J. Kim, K. W. Min, A. F. Nagy, and K. I. Oyama (1998), Effect of the magnetic field on the energetics of Mars ionosphere, *Geophys. Res. Lett.*, *25*, 2753–2756, doi:10.1029/98GL51839.

Connerney, J. E. P., J. Espley, P. Lawton, S. Murphy, J. Odom, R. Oliverson, and D. Sheppard (2015), The MAVEN magnetic field investigation, *Space Sci. Rev.*, *195*, 257–291, doi:10.1007/s11214-015-0169-4.

Cravens, T. E. (1997), *Physics of Solar System Plasmas*, Cambridge Univ. Press, Cambridge, U. K.

Cravens, T. E., A. F. Nagy, L. H. Brace, R. H. Chen, and W. C. Knudsen (1979), The energetics of the ionosphere of Venus: A preliminary model based on Pioneer Venus observations, *Geophys. Res. Lett.*, *6*, 341–344, doi:10.1029/GL006i005p00341.

Cravens, T. E., T. I. Gombosi, J. Kozyra, A. F. Nagy, L. H. Brace, and W. C. Knudsen (1980), Model calculations of the dayside ionosphere of Venus: Energetics, *J. Geophys. Res.*, *85*, 7778–7786, doi:10.1029/JA085iA13p07778.

Eparvier, F. G., P. C. Chamberlin, T. N. Woods, and E. M. B. Thiemann (2015), The solar extreme ultraviolet monitor for MAVEN, *Space Sci. Rev.*, *195*, 293–301, doi:10.1007/s11214-015-0195-2.

Ergun, R. E., M. W. Morooka, L. A. Andersson, C. M. Fowler, G. T. Delory, D. J. Andrews, A. I. Eriksson, T. McEnulty, and B. M. Jakosky (2015), Dayside electron temperature and density profiles at Mars: First results from the MAVEN Langmuir probe and waves instrument, *Geophys. Res. Lett.*, *42*, 8846–8853, doi:10.1002/2015GL065280.

Fontenla, J. M., J. Harder, W. Livingston, M. Snow, and T. Woods (2011), High-resolution solar spectral irradiance from extreme ultraviolet to far infrared, *J. Geophys. Res.*, *116*, D20108, doi:10.1029/2011JD016032.

Fox, J. L., and A. B. Hać (2009), Photochemical escape of oxygen from Mars: A comparison of the exobase approximation to a Monte Carlo method, *Icarus*, *204*, 527–544, doi:10.1016/j.icarus.2009.07.005.

Fox, J. L., and A. Dalgarno (1979), Ionization, luminosity, and heating of the upper atmosphere of Mars, *J. Geophys. Res.*, *84*, 7315–7333, doi:10.1029/JA084iA12p07315.

Frahm, R. A., et al. (2006), Carbon dioxide photoelectron energy peaks at Mars, *Icarus*, *182*, 371–382, doi:10.1016/j.icarus.2006.01.014.

Gan, L., T. E. Cravens, and M. Horanyi (1990), Electrons in the ionopause boundary layer of Venus, *J. Geophys. Res.*, *95*, 19,023–19,035, doi:10.1029/JA095iA11p19023.

Gan, L., C. N. Keller, and T. E. Cravens (1992), Electrons in the ionosphere of Titan, *J. Geophys. Res.*, *97*, 12,137–12,151, doi:10.1029/92JA00300.

Halekas, J. S., et al. (2015), MAVEN observations of solar wind hydrogen deposition in the atmosphere of Mars, *Geophys. Res. Lett.*, *42*, 8901–8909, doi:10.1002/2015GL064693.

Hanson, W. B., and G. P. Mantas (1988), Viking electron temperature measurements: Evidence of a magnetic field in the Martian ionosphere, *J. Geophys. Res.*, *93*, 7538–7544, doi:10.1029/JA093iA07p07538.

Hanson, W. B., S. Santatani, and D. R. Zuccaro (1977), The Martian ionosphere as observed by the Viking Retarding Potential Analyzer, *J. Geophys. Res.*, *82*, 4351–4363, doi:10.1029/JS082i028p04351.

Harada, Y., et al. (2015), Magnetic reconnection in the near-Mars magnetotail: MAVEN observations, *Geophys. Res. Lett.*, *42*, 8838–8845, doi:10.1002/2015GL065004.

Harada, Y., et al. (2016), MAVEN observations of energy-time dispersed electron signatures in Martian crustal magnetic fields, *Geophys. Res. Lett.*, *43*, 939–944, doi:10.1002/2015GL067040.

Itikawa, Y. (2002), Cross sections for electron collisions with carbon dioxide, *J. Phys. Chem. Ref. Data*, *31*, 749–767, doi:10.1063/1.1481879.

Itikawa, Y., and A. Ichimura (1990), Cross sections for collision of electrons and photons with atomic oxygen, *J. Phys. Chem. Ref. Data*, *19*, 637–651, doi:10.1063/1.555857.

Jakosky, B. M., et al. (2015), The Mars Atmosphere and Volatile Evolution (MAVEN) mission, *Space Sci. Rev.*, *195*, 3–48, doi:10.1007/s11214-015-0139-x.

Johnson, R. E. (1978), Comment on ion and electron temperatures in the Martian upper atmosphere, *Geophys. Res. Lett.*, *5*, 989–992, doi:10.1029/GL005i011p00989.

Krymskii, A. M., T. K. Breus, N. F. Ness, M. H. Acuña, J. E. P. Connerney, D. H. Crider, D. L. Mitchell, and S. J. Bauer (2002), Structure of the magnetic field fluxes connected with crustal magnetization and topside ionosphere at Mars, *J. Geophys. Res.*, *107*(A9), 1245, doi:10.1029/2001JA000239.

Liemohn, M. W., et al. (2006), Numerical interpretation of high-altitude photoelectron observations, *Icarus*, *182*, 383–395, doi:10.1016/j.icarus.2005.10.036.

Lillis, R. J., et al. (2015), Characterizing atmospheric escape from Mars today and through time, with MAVEN, *Space Sci. Rev.*, *195*, 357–422, doi:10.1007/s11214-015-0165-8.

Ma, Y., A. F. Nagy, K. C. Hansen, D. L. DeZeeuw, T. I. Gombosi, and K. G. Powell (2002), Three-dimensional multispecies MHD studies of the solar wind interaction with Mars in the presence of crustal fields, *J. Geophys. Res.*, *107*(A10), 1282, doi:10.1029/2002JA009293.

Ma, Y., A. F. Nagy, I. V. Sokolov, and K. C. Hansen (2004), Three-dimensional, multispecies, high spatial resolution MHD studies of the solar wind interaction with Mars, *J. Geophys. Res.*, *109*, A07211, doi:10.1029/2003JA010367.

Ma, Y., X. Fang, C. T. Russell, A. F. Nagy, G. Toth, J. G. Luhmann, D. A. Brain, and C. Dong (2014), Effects of crustal field rotation on the solar wind plasma interaction with Mars, *Geophys. Res. Lett.*, *41*, 6563–6569, doi:10.1002/2014GL060785.

Mahaffy, P. R., et al. (2015), The neutral gas and ion mass spectrometer on the Mars atmosphere and volatile evolution mission, *Space Sci. Rev.*, *195*, 49–73, doi:10.1007/s11214-014-0091-1.

Matta, M., M. Galand, L. Moore, M. Mendillo, and P. Withers (2014), Numerical simulations of ion and electron temperatures in the ionosphere of Mars: Multiple ions and diurnal variations, *Icarus*, *227*, 78–88, doi:10.1016/j.icarus.2013.09.006.

McFadden, J. P., et al. (2015), MAVEN SupraThermal and Thermal Ion Composition (STATIC) instrument, *Space Sci. Rev.*, *195*, 199–256, doi:10.1007/s11214-015-0175-6.

Mitchell, D. L., et al. (2016), The MAVEN Solar Wind Electron Analyzer, *Space Sci. Rev.*, *200*, 495–528, doi:10.1007/s11214-015-0232-1.

Mott-Smith, H. M., and I. Langmuir (1926), The theory of collectors in gaseous discharges, *Phys. Rev.*, *28*(4), 727–763, doi:10.1103/PhysRev.28.727.

Nagy, A. F., and P. M. Banks (1970), Photoelectron fluxes in the ionosphere, *J. Geophys. Res.*, *75*, 6260–6270, doi:10.1029/JA075i031p06260.

Nagy, A. F., and T. E. Cravens (1988), Hot oxygen atoms in the upper atmospheres of Venus and Mars, *Geophys. Res. Lett.*, *15*, 433–435, doi:10.1029/GL015i005p00433.

Ozak, N., T. E. Cravens, G. H. Jones, A. J. Coates, and I. P. Robertson (2012), Modeling of electron fluxes in the Enceladus plume, *J. Geophys. Res.*, *117*, A06220, doi:10.1029/2011JA017497.

Peverall, R., et al. (2001), Dissociative recombination and excitation of O_2^+: Cross sections, product yields and implications for studies of ionospheric airglows, *J. Chem. Phys.*, *114*, 6679–6689, doi:10.1063/1.1349079.

Rahmati, A., D. E. Larson, T. E. Cravens, R. J. Lillis, P. A. Dunn, J. S. Halekas, J. E. Connerney, F. G. Eparvier, E. M. B. Thiemann, and B. M. Jakosky (2015), MAVEN insights into oxygen pickup ions at Mars, *Geophys. Res. Lett.*, *42*, 8870–8876, doi:10.1002/2015GL065262.

Richard, M. S., T. E. Cravens, I. P. Robertson, J. H. Waite, J.-E. Wahlund, F. J. Crary, and A. J. Coates (2011), Energetics of Titan's ionosphere: Model comparisons with Cassini data, *J. Geophys. Res.*, *116*, A09310, doi:10.1029/2011JA016603.

Rohrbaugh, R. P., J. S. Nisbet, E. Bleuler, and J. R. Herman (1979), The effect of energetically produced O_2^+ on the ion temperatures of the Martian thermosphere, *J. Geophys. Res.*, *84*, 3327–3338, doi:10.1029/JA084iA07p03327.

Sakai, S., A. Rahmati, D. L. Mitchell, T. E. Cravens, S. W. Bougher, C. Mazelle, W. K. Peterson, F. G. Eparvier, J. M. Fontenla, and B. M. Jakosky (2015), Model insights into energetic photoelectrons measured at Mars by MAVEN, *Geophys. Res. Lett.*, *42*, 8894–8900, doi:10.1002/2015GL065169.

Schunk, R. W., and A. F. Nagy (2009), *Ionospheres: Physics, Plasma Physics, and Chemistry*, 2nd ed., Cambridge Univ. Press, Cambridge, U. K.

Singhal, R. P., and R. C. Whitten (1988), Thermal structure of the ionosphere of Mars: Simulations with one- and two-dimensional models, *Icarus*, *74*, 357–364, doi:10.1016/0019-1035(88)90048-6.